




Identification of an Altered Matrix Signature in Kidney Aging and Disease

Michael J. Randles,¹ Franziska Lausecker,¹ Qingyang Kong,² Hani Suleiman,³ Graeme Reid ⁴ Maria Kolatsi-Joannou,⁵ Bernard Davenport,¹ Pinyuan Tian,¹ Sara Falcone ⁶ Paul Potter,⁷ Tom Van Agtmael,⁸ Jill T. Norman,² David A. Long ⁵ Martin J. Humphries,¹ Jeffrey H. Miner,³ and Rachel Lennon^{1,9}

Due to the number of contributing authors, the affiliations are listed at the end of this article.

ABSTRACT

Background Accumulation of extracellular matrix in organs and tissues is a feature of both aging and disease. In the kidney, glomerulosclerosis and tubulointerstitial fibrosis accompany the decline in function, which current therapies cannot address, leading to organ failure. Although histologic and ultrastructural patterns of excess matrix form the basis of human disease classifications, a comprehensive molecular resolution of abnormal matrix is lacking.

Methods Using mass spectrometry-based proteomics, we resolved matrix composition over age in mouse models of kidney disease. We compared the changes in mice with a global characterization of human kidney matrix during aging and to existing kidney disease datasets to identify common molecular features.

Results Ultrastructural changes in basement membranes are associated with altered cell adhesion and metabolic processes and with distinct matrix proteomes during aging and kidney disease progression in mice. Within the altered matrix, basement membrane components (laminins, type IV collagen, type XVIII collagen) were reduced and interstitial matrix proteins (collagens I, III, VI, and XV; fibrinogens; and nephrolectin) were increased, a pattern also seen in human kidney aging. Indeed, this signature of matrix proteins was consistently modulated across all age and disease comparisons, and the increase in interstitial matrix was also observed in human kidney disease datasets.

Conclusions This study provides deep molecular resolution of matrix accumulation in kidney aging and disease, and identifies a common signature of proteins that provides insight into mechanisms of response to kidney injury and repair.

JASN 32: 1713–1732, 2021. doi: <https://doi.org/10.1681/ASN.2020101442>

Extracellular matrix (ECM) is organized as basement membranes (BMs), which support continuous layers of cells, or as looser interstitial matrix.¹ In addition to providing a scaffold, ECM directs organ shape and sequesters growth factors and enzymes for controlled, outside-in signaling.² This extracellular environment is complex and dynamic, with >1000 matrisome proteins annotated.³ Matrix synthesis and turnover requires tight regulation for the maintenance of organ function, and matrix accumulation is associated with a wide spectrum of human disease. In the Western world, 45% of

Received October 12, 2020. Accepted March 22, 2021.

M.J.R. and F.L. contributed equally to this work.

Published online ahead of print. Publication date available at www.jasn.org.

Present address: Dr. Michael J. Randles, Faculty of Medicine, and Life Sciences, Chester Medical School, University of Chester, Chester CH14AR, United Kingdom.

Correspondence: Prof. Rachel Lennon, Wellcome Centre for Cell-Matrix Research, Michael Smith Building, Oxford Road, University of Manchester, M13 9P T, United Kingdom. Email: Rachel.Lennon@manchester.ac.uk

Copyright © 2021 by the American Society of Nephrology

deaths have been associated with organ fibrosis.⁴ Thus, understanding the drivers of matrix accumulation is key to identifying strategies to prolong organ survival.

Excess matrix is seen across a wide spectrum of pathology and is incorporated into the histologic and ultrastructural descriptions of many diseases.⁵ In the kidney, glomerulosclerosis is a feature of aging, and glomerular disease⁶ and tubulointerstitial (TI) fibrosis is seen with both primary tubular disease and as a consequence of glomerular disease^{7,8}; however, the comprehensive molecular definition of altered matrix is limited. Using proteomics to define global protein composition has improved the resolution of matrix complexity, and this includes the human glomerular matrisome, which contains >140 structural and regulatory components.^{9,10} Proteomic studies in kidney disease have also revealed changes in matrix composition,^{11,12} but these have been limited by sample volume and have not used matrix-enrichment strategies, which improve resolution.¹³

Along the nephron, there is distinct matrix composition within BMs and interstitial matrices.¹⁴ BMs underlie parietal epithelial cells, separate endothelial cells from overlying podocytes, provide a scaffold for tubular epithelial cells, and form an integral component of blood vessel walls in the kidney. Interstitial matrices include the mesangial matrix and the loose TI matrix. The glomerular and tubular segments of the nephron have distinct functions, and their differential matrix composition is likely to reflect their underlying functions, including filtration and reabsorption. One example of structure supporting function is the triple helix of type IV collagen protomers, which may resist mechanical load¹⁵ and could explain the distinct localization of collagen IV isoforms along the nephron.

Here, we performed deep proteomic profiling to define global changes in kidney matrix and to identify common components and pathways. In mouse models of genetic defects in collagen IV, we found distinct structural abnormalities of the matrix, associated with altered cell adhesion and metabolic processes, and a signature of abnormal matrix composition. In young and aged human kidneys and existing kidney disease datasets, we identified a similar signature of altered matrix. Broadly, we observed a reduction in BM components and an increase in interstitial matrix proteins in both mouse models and human tissue.

METHODS

Antibodies

Primary antibodies were diluted in a blocking buffer (1% donkey serum, 2% BSA, 0.1% Triton X-100 in PBS). We used primary antibodies against type VI collagen (ab6588; Abcam) at a dilution of 1:100 and 1:500 for stochastic optical reconstruction microscopy (STORM) imaging; the type IV collagen chains $\alpha 1$, $\alpha 2$, $\alpha 3$, $\alpha 4$, $\alpha 5$, and $\alpha 6$ (7070, 7071, 7076, 7073, 7077, and 7074, respectively; Chondrex, Woodinville, WA) at a dilution of 1:200; type I collagen (OAR-AO2579; Gentaur, Kapenhout, Belgium) at a dilution of

Significance Statement

Abnormal extracellular matrix is a histologic feature of kidney aging and disease. However, a comprehensive molecular basis for altered matrix is not well understood. Ultrastructural and proteomic studies in mouse models of genetic kidney disease and human tissue define a molecular basis for altered matrix, which has common features across aging and disease progression. Broadly, basement membrane components are reduced, interstitial matrix proteins are increased, and this is coupled with altered cell adhesion and metabolic processes. Furthermore, a signature of altered matrix proteins appears before ultrastructural defects and could have utility as biomarkers of kidney health. Mechanistically, this altered kidney matrix may initiate abnormal kidney cell–matrix and immune cell–matrix interactions, which therapy could target.

1:100; podocin (ab50339; Abcam) at a dilution of 1:400; fibulin-1 (sc-25281; Santa Cruz Biotechnology, Dallas, TX) at a dilution of 1:100; nidogen/entactin antibody (MAB1946, ELM1; Merck, Darmstadt, Germany) at a dilution of 1:100; laminin- $\beta 2$ (ab210956; Abcam) at a dilution of 1:100; Tinag (ab67614; abcam) at a dilution of 1:100; and integrin $\beta 1$ (clone 9EG7; BD Pharmingen) at a dilution of 1:500. We used secondary antibodies conjugated to Alexa Fluor 488 or 594 (Life Technologies) for immunofluorescence.

Mice

We used *Col4a1*^{+/*SVC*} mice, which carry a point mutation causing an amino acid substitution (G1064D).¹⁶ These mice were on a BL6/C57 background. We used littermate controls, male mice for phenotypic consistency, and three mice from each group for proteomic analysis. *Col4a3*^{-/-} mice were generated as described.¹⁷ In brief, the first three exons of the carboxy-terminal (NC1) domain of collagen- $\alpha 3$ (IV) chain were deleted, causing absence of collagen- $\alpha 3$ (IV) protein. *Col4a5*^{-/-} mice were obtained from the International Mouse Phenotyping Consortium.¹⁸ The line was generated by deletion of the critical exon 36, resulting in the absence of the collagen- $\alpha 5$ (IV) protein, using the published allele map.¹⁹ *Col4a3*^{-/-} and *Col4a5*^{-/-} mice were on a BL6/C57 background. We used littermate controls, male mice for phenotypic consistency, and five mice from each group for proteomic analysis. All experiments were performed in compliance with the Animals (Scientific Procedures) Act 1986 regulations of the United Kingdom Home Office.

Glomerular Isolation from Mice

Cortical tissue was dissected from frozen-thawed kidney, placed in a glass dish, and cut into small pieces ($\leq 1 \text{ mm}^3$) as previously described.⁹ Tissue pieces were washed three times with PBS. Tissue pieces were transferred onto a 100- μm cell strainer (Falcon) and mechanically disintegrated. We then added PBS and collected the flow through. The resulting tissue solution was filtered through a 70- μm cell strainer (Falcon). Glomeruli were caught on the 70- μm cell strainer.

The cell strainer was inverted and caught glomeruli were washed off the sieve and collected in a container.

Human Kidney

Human kidneys ($n=6$) anatomically unsuitable for transplantation, and with no recorded comorbidities, were collected under ethical approval (regional ethics committee approval identifiers 05/Q0508/6 [University College London] and 06/Q1406/38 [Manchester]). Samples were grouped into young (15, 29, 37 years) and aged (61, 67, 69 years) kidneys, with $n=3$ per group. Five of the six kidneys were from male donors, and the sex of the kidney from the 67 year old was not recorded. We also used kidney biopsy sections from a male patient presenting at age 14 years with CKD stage 3, due to autosomal recessive (*COL4A3*) Alport syndrome, and control kidney tissue (nonaffected tissue of tumor nephrectomy), with the ethical approval identifier 06/Q1406/38 (Manchester).

Glomerular and TI Isolation from Human Kidney

Cortical tissue (2 g) was dissected from frozen-thawed kidney, placed in a glass dish, and cut into small pieces ($\leq 1 \text{ mm}^3$) as previously described.⁹ Graded sieves of 250, 150, and 106 μm were assembled, with the 250- μm sieve at the top, and placed on a collection container. Tissue pieces were transferred onto the largest sieve in 5 ml of ice-cold PBS (without calcium and magnesium). We used the plunger from a 10-ml syringe to press the sample through the sieves. Fragments were washed through the sieves with 60–100 ml of ice-cold PBS. Glomeruli were retained on 150- and 106- μm sieves, and were collected by inverting the sieves and washing with 20 ml of ice-cold PBS. Cortical TI fragments were retrieved from the collection container. The glomeruli and TI samples were centrifuged at $3000 \times g$ for 3 minutes at 4°C , washed three times by centrifugation, and then resuspended in 10 ml of ice-cold PBS. After the final wash, samples were resuspended in 5 ml PBS and aliquoted into five 1-ml aliquots. One aliquot from each sample was viewed under a light microscope to confirm the separation of glomeruli and TI tissue. One aliquot was frozen at -20°C for ECM enrichment, and the remainder was stored at -80°C .

Matrix Enrichment

Samples stored at -20°C were defrosted at room temperature, homogenized using a 21G needle and 2-ml syringe, and centrifuged at $14,000 \times g$ for 5 minutes at room temperature. We added 500 μl of ice-cold buffer solution 1 (10 mM Tris, 150 mM sodium chloride, 25 mM EDTA, 1% vol/vol Triton X-100, 25 $\mu\text{g/ml}$ leupeptin, 25 $\mu\text{g/ml}$ aprotinin, 0.5 mM 4-[2-aminoethyl]benzenesulfonyl fluoride hydrochloride) to the pellet and incubated the samples on ice for 1 hour. Samples were centrifuged at $14,000 \times g$ for 10 minutes at 4°C , and the supernatant was collected and mixed with 125 μl recovery buffer (15% wt/vol SDS, 100 mM 1,4-dithiothreitol, 200 mM Tris, 30% vol/vol glycerol, 0.01% bromophenol blue). This sample was designated soluble fraction 1 (most of the cellular

compartment) and stored at -80°C . The pellet was resuspended in 500 μl ice-cold buffer solution 2 (20 mM ammonium hydroxide, 0.5% vol/vol Triton X-100) and incubated on ice for 1 hour. Samples were centrifuged at $14,000 \times g$ for 10 minutes at 4°C and the supernatant was collected and designated soluble fraction 2. The pellet was resuspended in 500 μl PBS with DNase I (25 $\mu\text{g/ml}$) and incubated for 30 minutes at room temperature. Samples were centrifuged at $14,000 \times g$ for 10 minutes at 4°C , and the collected supernatant was designated soluble fraction 3. The final pellet was resuspended in a sample buffer and incubated for 10 minutes at 95°C to generate the ECM-enriched fraction.

Mass Spectrometry Data Acquisition

After SDS-PAGE, gel lanes were sliced and subjected to in-gel digestion with trypsin,²⁰ with modifications.²¹ Peptide samples were analyzed by liquid chromatography–tandem mass spectrometry using a nanoACQUITY UltraPerformance LC system (Waters) coupled online to an LTQ Velos mass spectrometer (Thermo Fisher Scientific), or an UltiMate 3000 Rapid Separation LC system (Thermo Fisher Scientific) coupled online to an Orbitrap Elite mass spectrometer (Thermo Fisher Scientific). Peptides were concentrated and desalted on a Symmetry C18 preparative column (20 mm \times 180 μm , 5- μm particle size; Waters) and separated on a bridged ethylene hybrid C18 analytical column (250 mm \times 75 μm , 1.7- μm particle size; Waters), using a 45-minute linear gradient from 1%–25% or 8%–33% (vol/vol) acetonitrile in 0.1% (vol/vol) formic acid at a flow rate of 200 nl/min. Peptides were selected for fragmentation automatically by data-dependent analysis.

Mass Spectrometry Identifications

Tandem mass spectra were extracted using extract_msn (Thermo Fisher Scientific) executed in Mascot Daemon (version 2.5.1; Matrix Science). Peak list files were searched against a modified version of the Uniprot mouse database (April 2016 database selected for *Mus musculus*) for mouse datasets, or Uniprot human database (November 2015 database selected for *Homo sapiens*) for human datasets. We set carbamidomethylation of cysteine as a fixed modification; oxidation of methionine and hydroxylation of proline and lysine were allowed as variable modifications. Only tryptic peptides were considered, with up to one missed cleavage permitted. Monoisotopic precursor mass values were used, and only doubly and triply charged precursor ions were considered. The mass tolerances for precursor and fragment ions were 5 ppm and 0.5 Da, respectively.

Mass Spectrometry Quantification

We used peptide intensity to calculate relative protein abundance. Orbitrap mass spectrometry data were entered into Progenesis LC-MS (Nonlinear Dynamics Ltd.) and automatically aligned. Spectra were extracted using extract_msn executed in Mascot Daemon (version 2.5.1) and imported back

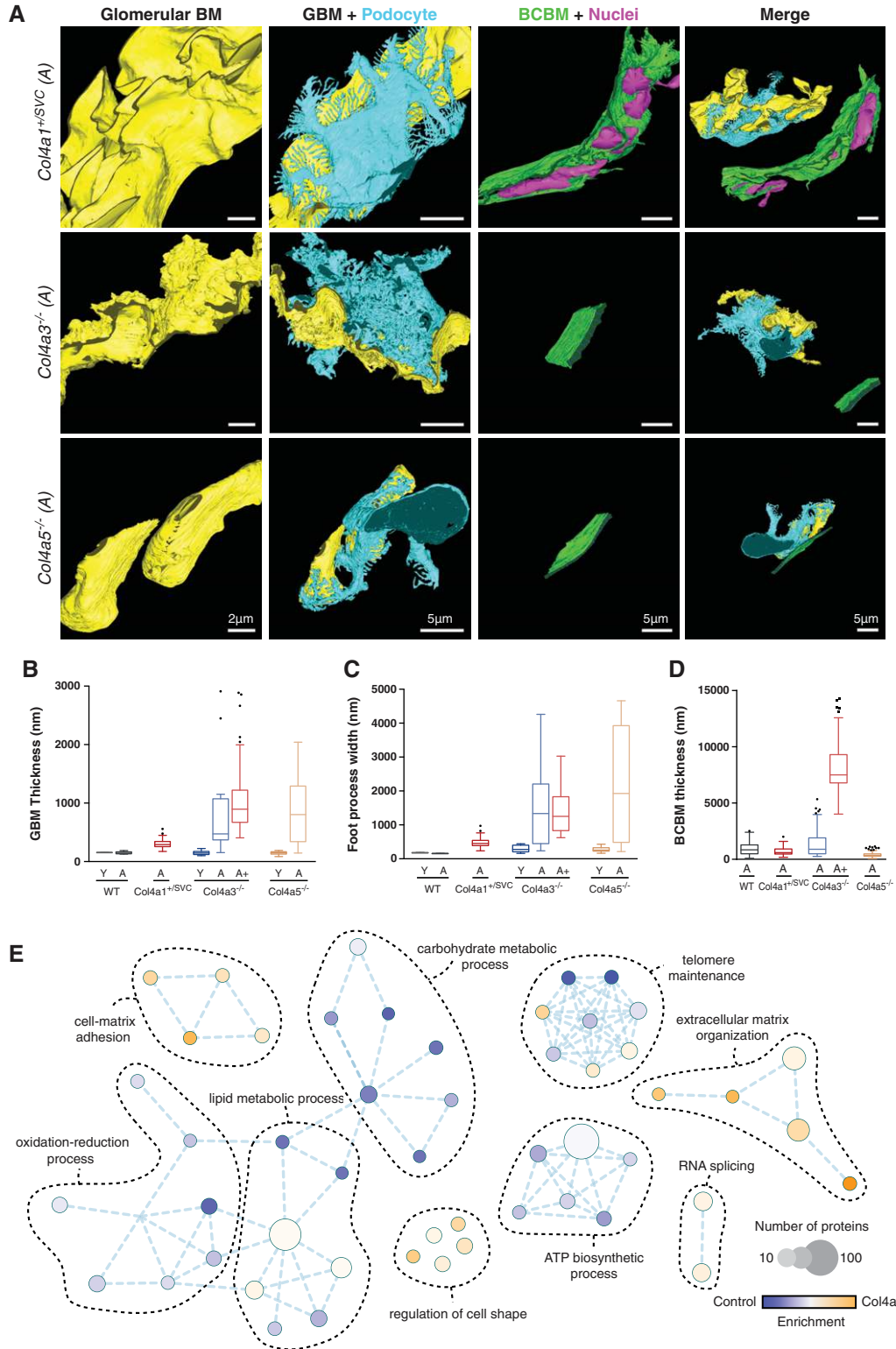


Figure 1. Identification of glomerular basement membrane and Bowman's capsule abnormalities in *Col4a* mutant mice. (A) Segmentation and modeling of serial block-face scanning electron microscopy data. Glomerular structure is visualized in Alport (*Col4a3^{-/-}* and *Col4a5^{-/-}*) and *Col4a1^{+SVC}* mice. *Col4a1^{+SVC}* mice demonstrated splitting of Bowman's capsule with enclosed nuclei. *Col4a3^{-/-}* mice presented irregular GBM and progressive thickening of Bowman's capsule, whereas Bowman's capsule was conserved in the *Col4a5^{-/-}* Alport mouse model. GBM (yellow), podocyte cell body with foot processes (light blue), and Bowman's capsule BM (green) were reconstructed. Dark blue lines highlight the thickness of the Bowman's capsule BM. Nuclei of cells intercalating the BM in *Col4a1^{+SVC}* are highlighted in pink. The analyzed *Col4a1^{+SVC}* mice received treatment with 4-sodium phenyl butyric

into Progenesis LC-MS to acquire intensity data. Chromatograms were aligned using the automatic alignment algorithm, followed by manual validation and adjustment of the aligned chromatograms. All features were used for peptide identifications. Progenesis LC-MS created the peak list file that was exported and searched in Mascot. Hi-N was used to infer protein abundance, using the three most abundant peptides.²² We then exported peptide and protein data from Progenesis LC-MS as .csv files to be analyzed in Excel (Microsoft). Proteins identified by one unique peptide, and a Mascot score indicating a <5% false discovery rate, were considered to be part of the definition of the human TI matrisome. The data were further filtered to include only proteins present in two out of three TI samples in a specific age group. Proteins identified by three unique peptides and a Mascot score indicating a <5% false discovery rate were considered for quantitative analysis. We inferred protein abundance from normalized peptide intensities, using the “three most abundant unique Hi-N peptides” setting in Progenesis. Conflicts were resolved using protein grouping. To compare group protein abundances across samples, we used ANOVA with *post hoc* Bonferroni protein lists are shown in Supplemental Tables 1 and 2. To enable Gene Ontology (GO) lists with sufficiently large numbers of proteins in all comparisons, proteins with $P < 0.1$ and 1.4-fold increased or decreased abundance were taken forward for further analysis.

Protein Interaction Network Analysis

Cytoscape (version 3.7.2) was used for protein interaction network analysis. Matrisome proteins were selected from the Matrisome Project,³ and proteins identified in at least two biologic replicates were mapped onto a merged human, mouse, and rat interactome. This was built from the PICKLE 2.5 (released November 15, 2019; based on IntAct release 227/2019-11-04, BioGRID release 3.5.178, DIP release 20170205, and Human Protein Reference Database release 9) database merged with a matrix protein-specific interactome from the Protein Interaction Network Analysis platform; the *H. sapiens* network (release date, December 10, 2012); *M. musculus* network (release date, December 10, 2012); the *Rattus norvegicus* network (release date, December 10, 2012); the ECM interactions database MatrixDB (release date, April 20, 2012); and a literature-curated database of integrin-based, adhesion-associated proteins.²³ For networks where enrichment/fold change is presented, Progenesis LC-MS-normalized intensity data were used. Networks were manually grouped.

acid, as described previously, which did not affect the kidney phenotype.³³ Quantification of (B) GBM thickness, (C) podocyte foot process width, and (D) Bowman’s capsule BM (BCBM) thickness. Young (Y) mice were aged 6–8 weeks, adult (A) mice were 16–18 weeks old, and aged (A+) mice were 28 weeks old. Box-and-whisker plots represent the median, where the box represents interquartile range and whiskers represent the tenth to 90th percentile. $n = 1$ biologic sample per model. (E) GO enrichment map analysis was performed on 719 proteins detected by mass spectrometry with altered abundance (>1.4-fold; $P < 0.1$) in *Col4a1^{+ /svc}*, *Col4a3^{- /-}*, and *Col4a5^{- /-}* mice at all analyzed ages compared with aged-matched control mice. Over-represented biological processes are presented as nodes, and color represents Bonferroni-corrected P value (the lower the P value, the more intense the node color). Edge weight represents the overlap between the proteins in the connected nodes. $n = 5$ biologic samples per mouse model studied. WT, wild type.

Data Analysis

DAVID (version 6.7) was used for functional enrichment analysis. Keywords with fold enrichment ≥ 1.5 , Bonferroni-corrected $P < 0.05$, EASE score (modified Fisher exact test) of < 0.05 , and at least two proteins per keyword were considered significantly over-represented. We generated enrichment maps using all changed proteins detected, $P < 0.1$, and fold change at least > 1.4 . Enrichment maps were clustered using the clusterMaker application with Markov clustering algorithm tuning, and a granularity parameter of 2.5. Principal component analysis (PCA) was performed using MATLAB (version R2019a; MathWorks). Hierarchically clustered heat maps were generated on the basis of uncentered, Euclidean complete-linkage clustering in MultiExperiment Viewer (version 4.8.1). For clustered heat maps where the z-score or fold change is presented, we used Progenesis LC-MS-normalized intensity data.

Nephroseq Analysis

We used Nephroseq version 5 for analysis. Signature matrix proteins were searched for their fold change in gene expression in disease datasets compared with associated control samples. The following filters were applied: tissue type, glomeruli and analysis type, disease versus control analyses. Microarray data were extracted with the P value selection “all” and fold change “all.” The primary data are shown in Supplemental Table 3. Data that met the following criteria: $P < 0.05$, fold change = ± 1.5 are highlighted in orange in Supplemental Table 3 and taken forward for further analysis. Data are shown as box-and-whisker plots displaying all data points. The values below every plot indicate the number of datasets in which a transcript was detected out of all analyzed datasets (21 datasets). Data from the following datasets were extracted: Berthier Lupus Glom (analysis of lupus nephritis versus healthy living donor),²⁴ Hodgkin Diabetes Mouse Glom (analyses of diabetic nephropathy versus nondiabetic kidney [mouse model db/db C57BLKS], diabetic nephropathy versus nondiabetic kidney [mouse model DBA/2], and diabetic nephropathy versus nondiabetic kidney [mouse model eNOS-deficient C57BLKS db/db]),²⁵ Hodgkin FSGS Glom (analyses of collapsing FSGS versus normal kidney, FSGS versus normal kidney, and minimal change disease versus normal kidney),²⁶ Ju CKD Glom (analyses of arterial hypertension versus healthy living donor, diabetic nephropathy versus healthy living donor, FSGS versus healthy living donor, IgA nephropathy versus healthy living donor, lupus nephritis versus healthy living

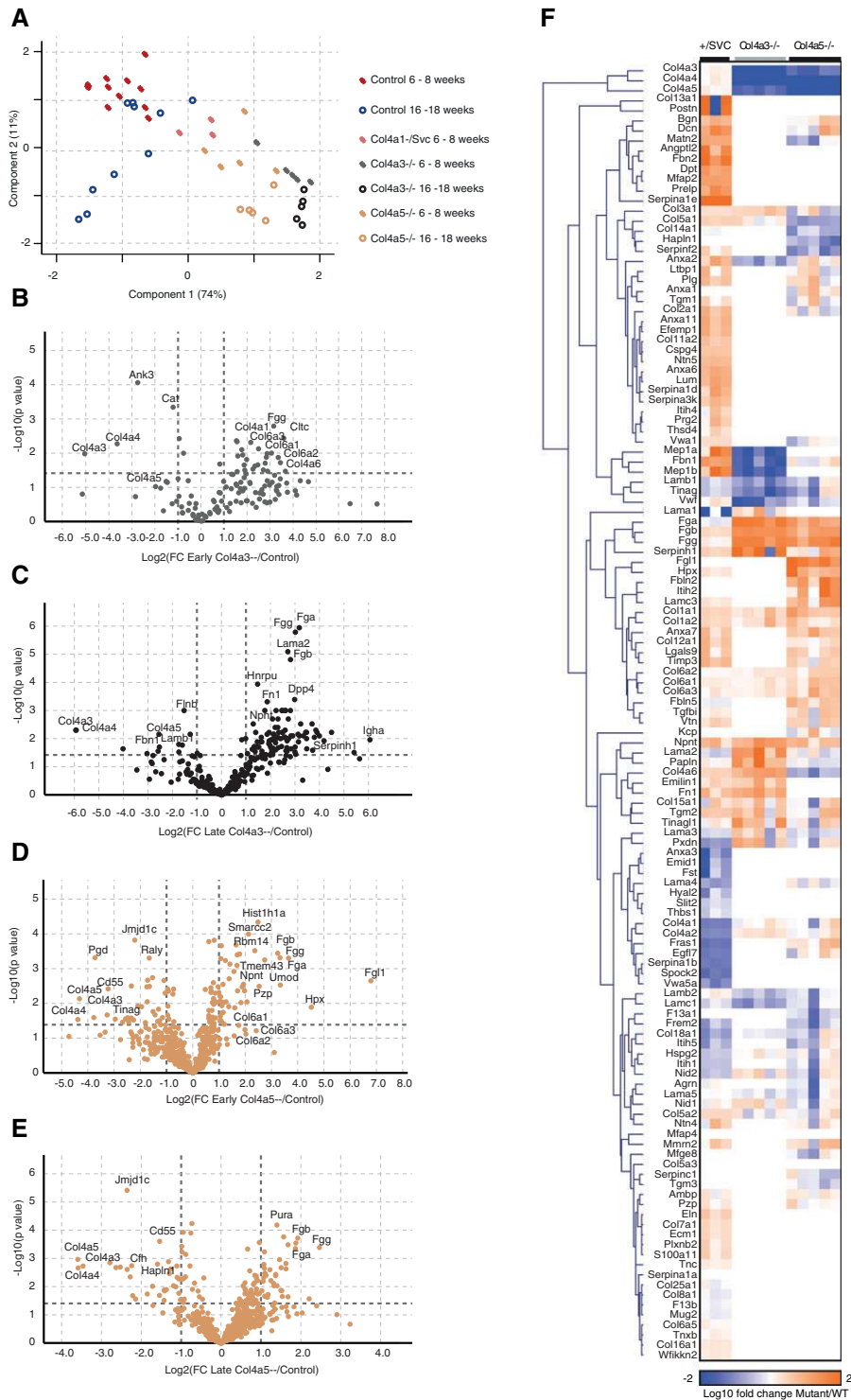


Figure 2. Changes in glomerular matrix composition are exacerbated with aging in *Col4a* mutant mice. Mouse glomerular extracts were fractionated to cellular and matrix fractions. All fractions were analyzed by mass spectrometry; proteins were identified with Mascot and quantified using Progenesis. (A) MATLAB was used for PCA of all detected proteins. Components 1 and 2 are presented; the percentage variance explained by component 1 is indicated on the x axis, and that of component 2 on the y axis. Samples were fractionated and the matrix fraction was further analyzed. (B–E) Volcano plots of proteins detected in matrix fractions demonstrate differential expression shown as \log_2 (fold change) compared with age-matched control on the x axis and $-\log_{10}(P$ value) on the y axis. (B) *Col4a3*^{-/-} mice at 6–8 weeks old, (C) *Col4a3*^{-/-} mice at 16–18 weeks, (D) *Col4a5*^{-/-} mice at 6–8 weeks old, and (E) *Col4a5*^{-/-} mice at 16–18 weeks old. (F) Detected matrix proteins at 6–8 weeks of age were clustered in MeV using Euclidean distance complete-linkage clustering. The clustered dendrogram is presented as a heat map, with orange representing increased abundance in *Col4a* mutant relative to control. FC, fold change; WT, wild type.

donor, minimal change disease versus healthy living donor, membranous glomerulonephropathy versus healthy living donor, tumor nephrectomy versus healthy living donor, thin BM disease versus healthy living donor, and vasculitis versus healthy living donor),²⁷ Neusser Hypertension Glom (analysis of nephrosclerosis versus tumor nephrectomy),²⁸ Peterson Lupus Glom (analysis of lupus nephritis versus normal kidney),²⁹ Reich IgAN Glom (analysis of IgA nephropathy versus healthy living donor),³⁰ and Woroniecka Diabetes Glom (analysis of diabetic nephropathy versus healthy living donor).³¹

Electron Microscopy

Samples were prepared as previously described.³² Briefly, mouse kidneys were harvested; immediately cut into 1 mm² pieces; and fixed in 2.5% glutaraldehyde, 4% paraformaldehyde (PFA), and 0.1 M HEPES, pH 7.4. Samples were stained in 1% osmium tetroxide and 1.5% potassium ferrocyanide in 0.1 M cacodylate buffer, followed by 1% thiocarbonylhydrazide. Samples were washed and stained further in 1% osmium tetroxide and incubated in 1% uranyl acetate overnight. Samples were incubated in lead aspartate (pH 5.5) for 1 hour at 60°C, dehydrated, and finally embedded in TAAB 812 hard resin. Samples were mounted onto an aluminum cryo pin. Block surfaces were trimmed using a glass knife or diamond trimming tool. To create a conductive surface, a gold coating was applied to the specimen. The samples were analyzed using a Quanta 250 FEG (FEI Company) and Gatan 3View system. The analyzed *Col4a1*^{+/*SVC*} mice received treatment with 4-sodium phenyl butyric acid, as described previously, which did not affect the kidney phenotype.³³ Kidney samples for transmission electron microscopy were fixed similarly as for serial block-face scanning electron microscopy. Sections (70–80 nm thick) were prepared and examined using a FEI Tecnai 12G2 Biotwin transmission electron microscope. Foot process width, glomerular BM (GBM) thickness, and Bowman's capsule BM thickness were measured using ImageJ (version 2.0.0-rc-68/1.52e). The foot process width was measured at the basal side of podocytes from ten different fields of view in the glomerulus. Measurements were taken from one glomerulus per mouse genotype. GBM thickness was measured radially from the endothelial side of the electron-dense GBM to the basal membrane of podocyte foot processes. Bowman's capsule thickness was measured radially in different sections of the acquired serial block-face scanning electron microscopy stack from one glomerulus.

Light Microscopy

We used formaldehyde-fixed, paraffin-embedded kidney sections for immunofluorescence. Images were acquired using a Zeiss Axioimager.D2 upright microscope, with a 20×/0.50 EC Plan-Neofluar objective, and captured using a Coolsnap HQ2 camera (Photometrics) through Micromanager software version 1.4.23. Images of stained cryosections were acquired using

a Zeiss AxioObserver Z1 wide-field microscope equipped with a 40×/EC Plan-Neofluar 1.3 Oil objective and an AxioCam MRm camera, controlled by Zeiss Axiovision software. Specific band pass filter sets for 4',6-diamidino-2-phenylindole, FITC, and Texas Red were used to prevent bleed through from one channel to the next. Images were processed and analyzed using ImageJ (versions 1.51j8 and 2.0.0-rc-68/1.52e). Total positive antibody fluorescence was measured in glomeruli and the TI separately and normalized to the total background in the same area to generate corrected total fluorescence. Background was subtracted using a rolling-ball algorithm in ImageJ in the immunofluorescence images.

Tissue Preparation and Staining for STORM Imaging

Tissue was fixed and stained as described previously.^{34,35} In brief, kidneys were fixed in 4% PFA in PBS. Samples were washed in PBS incubated in a cryoprotectant solution of 2.3 M sucrose plus 10% polyvinylpyrrolidone in 0.1 M piperazine-*N,N'*-bis(2-ethanesulfonic acid) at pH 7.2 at 4°C overnight. Tissue pieces were mounted on a metal sectioning pin and frozen in liquid nitrogen. Frozen tissue was sectioned using an EM-FC6 ultracryomicrotome (Leica) and collected on carbon-coated coverslips. Sections were fixed in 4% PFA for 20 minutes, washed with PBS, and PFA was quenched using 50 mM glycine in PBS. For immunofluorescence, sections were blocked in 2% BSA in PBS overnight, followed by another overnight incubation with primary antibodies diluted in 2% BSA in PBS. After washing, sections were incubated with secondary antibodies diluted in 2% BSA in PBS for 2 hours at room temperature. Secondary antibodies for direct STORM were purchased from Jackson ImmunoResearch Laboratories and custom conjugated to Andy Fluor 488, Cy3, or Cy5 reporter dyes, as described previously.³⁵ Sections were washed again in PBS and postfixed in 3% PFA plus 0.05% glutaraldehyde in PBS. After a final washing series, samples were imaged by Nikon N-STORM according to the manufacturer's instructions, as described previously.³⁵

Histology

Paraffin-embedded mouse tissue sections were stained using a Shandon Linistain GLX stainer (Thermo Fisher) for hematoxylin and eosin. Samples were mounted using Histokitt solution (Roth). For Picrosirius red staining, paraffin-embedded tissue sections were dewaxed using a Leica ST5010 autostainer. Tissue sections were stained by incubation of slides in Picrosirius red solution (0.5 g sirius red and 500 ml saturated aqueous solution of picric acid; Sigma) for 1 hour. Slides were washed in acidified water. Slides were dehydrated and mounted using Histokitt solution (Roth). Images were collected on an Olympus BX63 upright microscope, using a 60×/1.42 PlanApo N objective, and captured and white-balanced using a DP80 camera (Olympus) in color/polarized light mode through CellSens Dimension version 1.16 (Olympus). For TriPAS staining, paraffin sections were dewaxed and placed into 1% Periodic acid

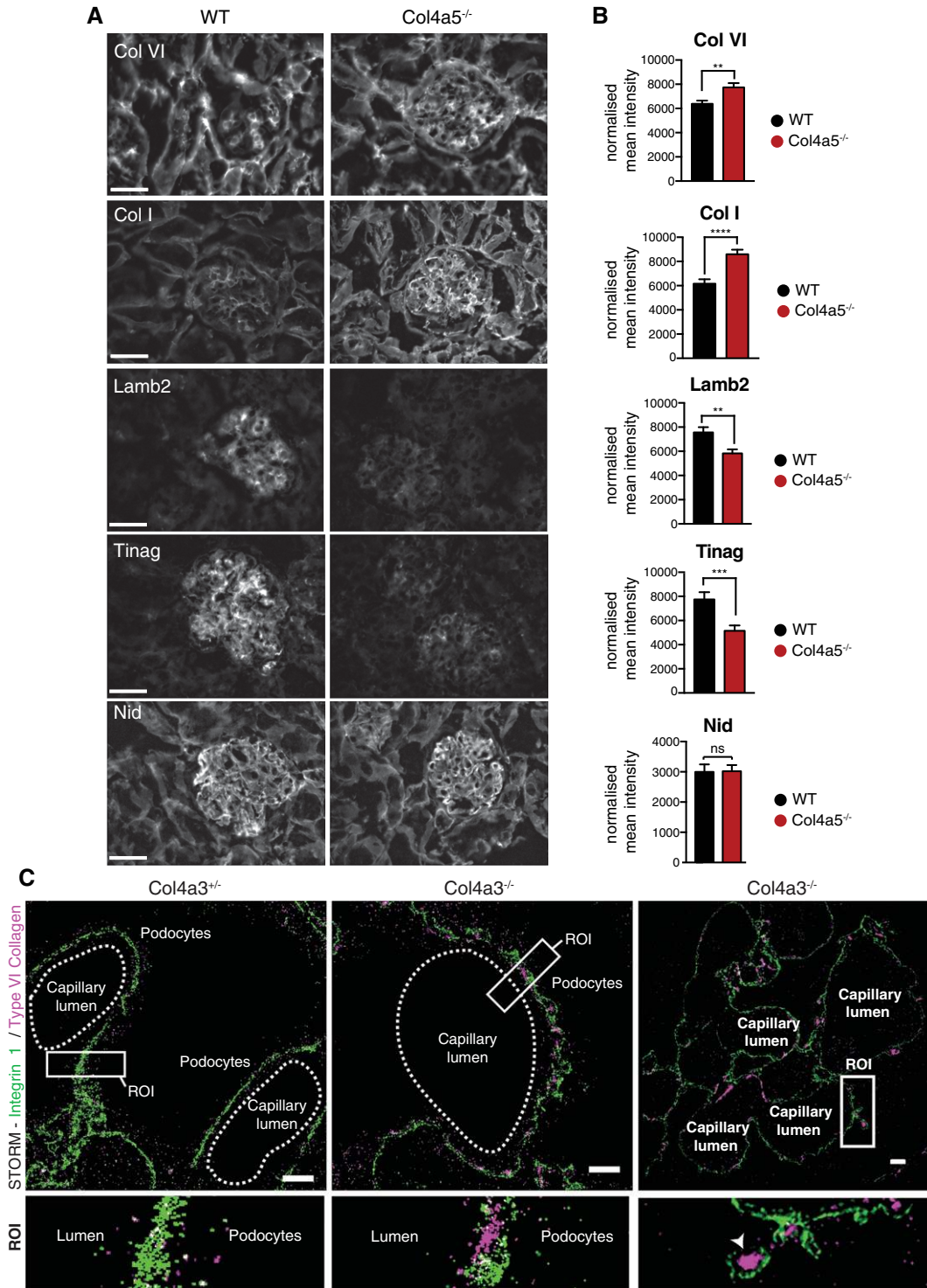


Figure 3. Imaging reveals altered matrix localization in Alport syndrome. Immunofluorescence demonstrated reduced BM proteins and increased interstitial matrix proteins in Alport mouse glomeruli. (A) Kidney sections of 8-week-old *Col4a5*^{-/-} and wild type (WT) mice were immunolabeled for collagen I (Col I), collagen VI, laminin-β2 (Lamb2), Tinag, and nidogen (Nid). (B) Quantification of (A). Mean fluorescence intensity was normalized to background and measured using ImageJ software. Images were acquired from *n*=4 mice per genotype and between ten and 15 glomeruli were analyzed per mouse, pooled data are shown. Background was subtracted from immunofluorescence images using a rolling-ball algorithm in ImageJ. (C) STORM was performed for integrin β1 (green) and collagen VI (purple) on *Col4a3*^{+/-} and *Col4a3*^{-/-} mouse sections. Region of interest (ROI) highlights collagen VI localization to the GBM in *Col4a3*^{-/-} glomeruli, specifically to areas of tickened GBM (arrowhead). Scale bars, 20 μm. ****P*<0.01, *****P*<0.001, ******P*<0.0001

for 10 minutes, and washed with tap and distilled water. Nuclei were stained with Gills No.2 hematoxylin for 1.5 minutes and washed in tepid tap water. Sections were stained in 2% orange G dissolved in 100 ml of 5% phosphotungstic acid for 1 minute. Sections were washed, dehydrated, and coverslips were applied. For human and mouse sections, a specialist kidney pathologist performed percentage glomerulosclerosis analysis and percentage interstitial fibrosis and tubular atrophy scoring on the TriPAS-stained tissue sections.

Urinary Albumin and Creatinine Analysis

Spot urine was collected at the same time of day for each group of mice. Urinary albumin was measured using a mouse albumin ELISA kit (E99-134; Bethyl Laboratories). Creatinine was measured using a creatinine ELISA assay according to the manufacturer's instructions (KGE005; R&D Systems).

Statistical Analyses

Data are presented as bar charts (mean \pm SEM) or box-and-whisker plots, and were analyzed using GraphPad Prism (version 7; GraphPad Software, La Jolla, CA). Data were analyzed using the Shapiro–Wilk test for normality and analyzed using the Kruskal–Wallis test or ANOVA with *post hoc* Bonferroni correction or *t* test, as appropriate. Statistical significance was accepted at $P < 0.05$. PCA was performed in MATLAB. Unsupervised hierarchic clustering was performed in T4MeV using a Euclidean, distance-based, complete-linkage matrix.

RESULTS

Structural and Compositional Change in Matrix

Type IV collagen is an essential component of BM in the kidney and exists as three networks comprised of $\alpha 1. \alpha 1. \alpha 2$ (IV), $\alpha 3. \alpha 4. \alpha 5$ (IV), and $\alpha 5. \alpha 5. \alpha 6$ (IV) heterotrimers. We confirmed the glomerular localization of these three networks with $\alpha 1. \alpha 1. \alpha 2$ (IV) in the mesangium, GBM, and Bowman's capsule; $\alpha 3. \alpha 4. \alpha 5$ (IV) in the GBM; and $\alpha 5. \alpha 5. \alpha 6$ (IV) in Bowman's capsule (Supplemental Figure 1). To understand the effect of glomerular disease on matrix, we investigated three mouse models with defects in the different collagen IV heterotrimers. First, *Col4a1*^{+/*svc*} mice that harbor a glycine to aspartic acid variant (G1064D) and have phenotypic overlap with human *COL4A1* variants, including defects in Bowman's capsule, kidney cysts, and tubular dysfunction.^{33,36} Second, *Col4a3*^{-/-} mice (autosomal recessive Alport syndrome) that have progressive glomerular disease associated with GBM defects.¹⁷ Third, a new *Col4a5*^{-/-} model of X-linked Alport syndrome. We characterized the *Col4a5*^{-/-} mice and demonstrated abnormal GBM thickness, podocyte effacement, and progressive albuminuria (Supplemental Figure 2). To investigate the effect of *Col4a* defects on matrix ultrastructure, we performed serial block-face scanning electron microscopy of young (6–8 weeks), adult (16–18 weeks), and aged (28 weeks) mice

(Figure 1, A–D, and Supplemental Videos 1–4). GBM was similar to wild type in adult *Col4a1*^{+/*svc*} mice, but thickened in adult *Col4a3*^{-/-} and *Col4a5*^{-/-} mice. Podocyte foot process width was preserved in *Col4a1*^{+/*svc*} mice, but increased with age in *Col4a3*^{-/-} and *Col4a5*^{-/-} mice. Bowman's capsule BM thickness was increased in adult *Col4a3*^{-/-} mice compared with adult wild type and *Col4a5*^{-/-} mice, and markedly thickened in aged *Col4a3*^{-/-} mice (Supplemental Video 3). The Bowman's capsule BM of adult *Col4a1*^{+/*svc*} mice was of a normal thickness, but there was infiltration of parietal epithelial cells. Given these structural changes in the matrix, we analyzed matrix composition using mass spectrometry-based proteomics. To interrogate changes that precede—and also coincide with—ultrastructural changes, we analyzed glomerular proteomes in young and adult mice. We isolated glomeruli and separated cellular and matrix fractions from three *Col4a1*^{+/*svc*}, five *Col4a3*^{-/-}, and five *Col4a5*^{-/-} mice, and their respective littermate controls, as previously described.⁹ Proteins were taken forward if identified by three unique peptides, with a Mascot score indicating a <5% false discovery rate. GO enrichment analysis highlighted increases in cell matrix and cell adhesion ontologies and a reduction in mitochondrial and metabolic components in all three *Col4a* models, compared with controls (Supplemental Figure 1E). Equivalent analyses of individual *Col4a* datasets highlighted similar cellular pathways (Supplemental Figure 3A), and PCA demonstrated model and age segregation (Figure 2A). Taken together, these findings highlight both structural and compositional changes in matrix in models of glomerular disease.

Evolution of Altered Matrix in Aging and Disease

To explore the altered glomerular matrix, we focused on the matrix-enriched fractions in which 707 (*Col4a1*^{+/*svc*}), 334 (*Col4a3*^{-/-}), and 600 (*Col4a5*^{-/-}) proteins were detected. Volcano plots revealed age- and genotype-specific changes in protein identifications (Figure 2, B–E). In keeping with predictions based on genotype, collagen- $\alpha 1$ (IV) and collagen- $\alpha 2$ (IV) were reduced in *Col4a1*^{+/*svc*} glomeruli, but moderately increased in both *Col4a3*^{-/-} and *Col4a5*^{-/-} glomeruli (Figure 2F and Supplemental Figure 4A). In addition, both collagen- $\alpha 3. \alpha 4. \alpha 5$ (IV) and laminin 521 were reduced in *Col4a3*^{-/-} and *Col4a5*^{-/-} in contrast to *Col4a1*^{+/*svc*} glomeruli (Figure 2F and Supplemental Figure 4A), and immunofluorescence confirmed reduced levels of collagen- $\alpha 3$ (IV) and collagen- $\alpha 4$ (IV) in *Col4a5*^{-/-} mice (Supplemental Figure 4B). Although ultrastructure was preserved in young Alport mice (Figure 1), we observed altered matrix composition (Figure 2, B and D, and Supplemental Figures 5A and 6A), with a broad reduction in BM components and an increase in interstitial matrix. This pattern was exaggerated in the older mice (Figure 2, C and E, and Supplemental Figures 5B and 6B). Although less pronounced, there were also changes during aging in wild type mice, which showed reduced collagen IV and increased

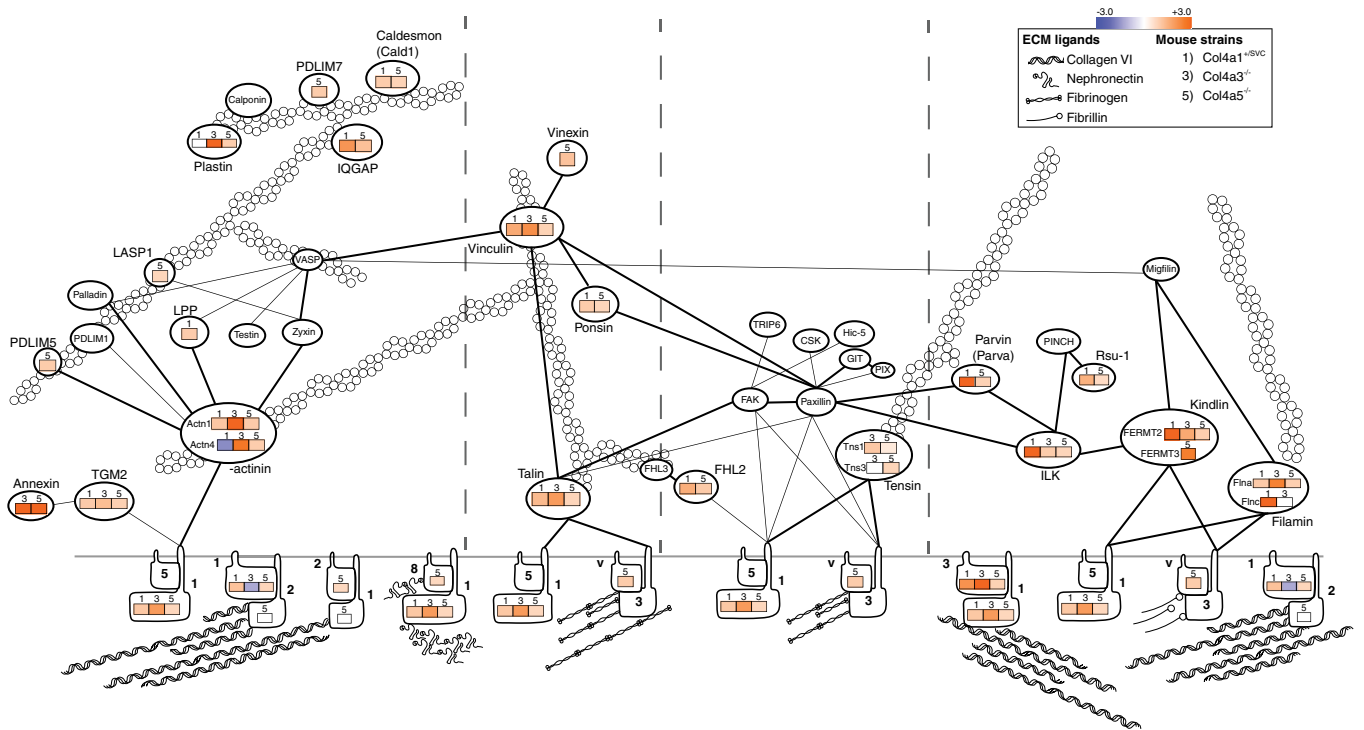


Figure 4. Protein abundance of cell-matrix adhesion components increases in *Col4a* mutants. Unsupervised hierarchical clustered heat map displaying the fold enrichment of adhesion proteins detected in 6- to 8-week-old *Col4a1^{+svvc}*, *Col4a3^{-/-}*, and *Col4a5^{-/-}* mass spectrometry datasets compared with their respective control. Orange represents increased (+) abundance in disease relative to control; blue represents decreased (-) abundance in disease relative to control. Adhesion proteins are displayed along the four different signaling axes to the actin cytoskeleton, as described previously.³⁸

collagen VI (Supplemental Figure 3B). We performed immunofluorescence on *Col4a5^{-/-}* kidney sections and also observed increased collagen VI and collagen I, and reduced laminin- β 2 and Tinag (Figure 3, A and B). For greater spatial resolution, we used STORM to determine the localization of increased collagen VI. Control, heterozygous *Col4a3^{+/-}* mice have normal kidney function,³⁷ and we detected regular integrin β 1 fluorescence and no GBM collagen VI. However, in *Col4a3^{-/-}* mice, we detected collagen VI in expanded regions of GBM (Figure 3C). Overall, we found altered matrix composition before overt ultrastructural changes, and these changes increased in aging and disease progression.

Increased Cell-Matrix Adhesion in Disease

To connect the altered matrix with cell-matrix adhesion, we used the consensus adhesome³⁸ to select integrin adhesion complex components from all three disease model datasets (Figure 4). The consensus adhesome is centered around four dominant signaling hubs: ILK-PINCH-kindlin, FAK-paxillin, talin-vinculin, and α -actinin-zyxin-VASP. When examining proteins detected in cellular and matrix fractions across these hubs, we found a global increase in abundance of integrin adhesion components and their respective ligands. In particular, we found parallel increases in the collagen binding integrins

(α 1 β 1, α 2 β 1) with collagen VI, collagen I, and collagen III, in addition to the parallel increase in α 8 β 1 and its ligand, nephronectin. The observed global increase in adhesion components may reflect a greater receptor-ligand interaction associated with podocyte efferment.

Altered Glomerular Matrix in Human Kidney Aging

Having observed altered matrix in aging and disease in mice, we examined human tissue. Glomerulosclerosis, tubular atrophy, and interstitial fibrosis are observed in human aging.^{39,40} Therefore, we investigated changes in matrix over age in unused human donor kidneys. Sections of young (15, 29, 37 years) and older (61, 67, 69 years) human kidneys were assessed blindly by a kidney pathologist, who reported occasional focal glomerular and interstitial damage, consistent with age. From these kidneys, glomeruli were isolated, subjected to matrix fractionation, and analyzed by mass spectrometry. PCA of matrix proteins showed good separation by age (Figure 5A), and GO enrichment analysis of all detected proteins highlighted matrix and cell-matrix ontologies (Supplemental Figure 7A). Volcano plots and hierarchical clustering highlighted glomerular matrix proteins changing with age (Figure 5, B and C). There was a skewed distribution with a greater number of increased abundance proteins in aged samples, including

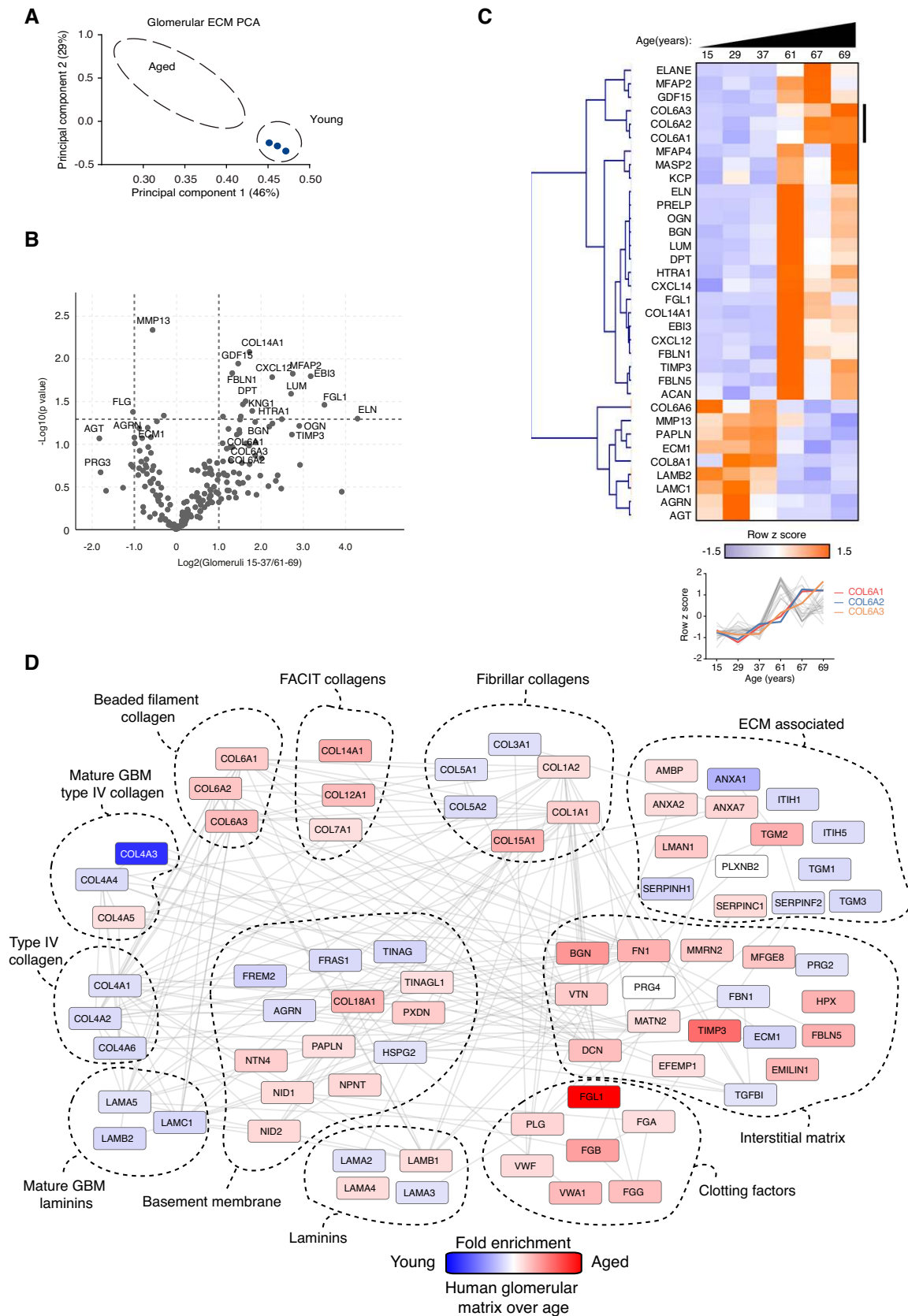


Figure 5. Human aging is associated with marked alterations in glomerular matrix composition. Glomeruli were isolated from young (15, 29, 37 years) and aged (61, 67, 69 years) human kidneys, subjected to matrix fractionation, and analyzed by mass spectrometry. (A)

collagen VI and TIMP3 (Figure 5B). Fewer proteins were enriched in younger glomeruli, including flaggrin-2, ECM1, and agrin. Protein-protein network mapping highlighted a reduction in BM components, including laminins and collagen IV, and an increase in interstitial matrix proteins (Figure 5D). Overall, these findings highlight altered composition of matrix during human glomerular aging, with similarity to aging and disease in mice.

Defining the Human TI Matrisome

Together with altered glomerular matrix in kidney aging and disease, there are changes in the tubulointerstitium.⁸ The matrix in this kidney compartment has received far less research attention; therefore, we first defined the human TI matrisome. We isolated TI matrix from six human kidneys (as above) for analysis by mass spectrometry. We included proteins identified by one unique peptide, a Mascot score indicating a <5% false discovery rate, and being present in two out of three samples in each age group. We robustly identified 141 proteins (Supplemental Figure 8, A and B, and Supplemental Table 2), and 90% of all of the components were also found in the glomerular matrix from this study and our previous investigation.⁹ Comparison of human glomerular and TI matrix revealed distinct proteomes (Supplemental Figure 8C). Collagen- $\alpha 3(\text{IV})$ was abundant in the glomerular matrix, but also detected in the tubulointerstitium, which we validated by immunofluorescence (Supplemental Figure 9A). We screened the Human Protein Atlas⁴¹ to confirm localization of 67 components in the tubulointerstitium and 80 in both glomerular and TI compartments (Supplemental Figure 9, B and C). By combining the glomerular and TI datasets, we defined the combined human kidney matrisome, dominated by proteoglycans, collagens, and a wide variety of matrix regulators and secreted factors (Supplemental Figure 10). Together, these data highlight the complexity of the TI matrix and key compositional differences with the adjacent glomerular compartment.

Altered TI Matrix in Human Kidney Aging

After defining the human TI matrisome, we compared TI matrices from young (15, 29, 37 years) and aged (61, 67, 69 years) human kidneys. GO enrichment map analysis of all proteins highlighted increased matrix and cell-matrix adhesion ontologies, and a reduction in mitochondrial components

(Figure 6A). We found age-associated increases in the structural components collagen VI, fibulin-1, and fibronectin, and the matrix regulators TIMP3 and ADAMTS5 (Figure 6B). Indeed, several fibulin isoforms were increased in our mouse and human datasets, and immunofluorescence confirmed increased fibulin-1 in the tubulointerstitium (Figure 6, C and D). Furthermore, a number of age-related changes were found in both glomerular and TI matrix, including fibulin-1, TIMP3, and collagen VI (Figure 7, A and B). There were also distinct compartment changes, with reduced BM components observed in glomerular aging but not seen in the aged TI matrix, suggesting tubular BMs are less exposed to damage during aging. When relating these molecular changes to histology, we observed that aging was only accompanied by a small increase in glomerulosclerosis and interstitial fibrosis and tubular atrophy scores (Figure 7, C and D), in keeping with our finding in the mouse disease models that altered matrix composition precedes overt or widespread structural changes.

A Signature of Altered Kidney Matrix in Aging and Disease

Across our aging and disease datasets, we observed consistent increases in collagen VI, nephronectin, and fibrinogens, and decreased BM components (Figure 8, A and B). To investigate the relevance in human disease, we examined kidney biopsy sections from a young male patient with autosomal recessive Alport syndrome. Compared with control kidney sections, we observed increased levels of collagen VI and decreased levels of laminin- $\beta 2$ in the glomerulus (Figure 8C). To determine whether this signature applied to a wider spectrum of human kidney disease, we searched for the signature proteins in published proteomic datasets. In a study of IgA nephropathy,¹¹ we found concordant increases in collagen VI and fibrinogen chains and, in diabetic kidney disease (DKD),¹² there was increased collagen VI and nephronectin (Figure 8D). Data from a biopsy specimen study of human FSGS identified increased interstitial collagen XV and Tgm2.⁴² We also observed reduced BM components in IgA nephropathy and FSGS, but not in DKD (Figure 8D), which may reflect the overall matrix expansion seen in DKD. To provide insight into the pathways associated with the matrix signature proteins, we created a one-hop interaction network by connecting upregulated signature proteins with their nearest neighbors identified in protein interaction databases (Supplemental Figure 11). This

MATLAB was used for PCA of matrisome proteins. Components 1 and 2 are presented and the percentage variance explained by each component is indicated on the relevant axis. (B) Volcano plots of proteins detected in matrix fractions demonstrate differential protein abundance shown as the $\log_2(\text{fold change})$ of aged over young glomeruli on the x axis and $-\log_{10}(P \text{ value})$ on the y axis. (C) Unsupervised hierarchical clustered heat map displaying ECM proteins detected in young and aged glomerular datasets. Data were standardized by row z-score and grouped in MeV using Pearson correlation complete-linkage clustering. Inset line graph shows increased type VI collagen protein abundance with age. (D) Protein-protein interaction network of altered human glomerular matrisome proteins. Mass spectrometry data from matrix-enriched protein fractions were filtered for known matrisome proteins. These proteins were mapped onto a merged human, mouse, and rat interactome. Nodes represent proteins and the edges represent reported protein-protein interactions. Color represents fold enrichment to datasets, with increased abundance in aged human glomerular samples illustrated in red and increased abundance in young human glomerular samples illustrated in blue. Proteins are grouped by function.

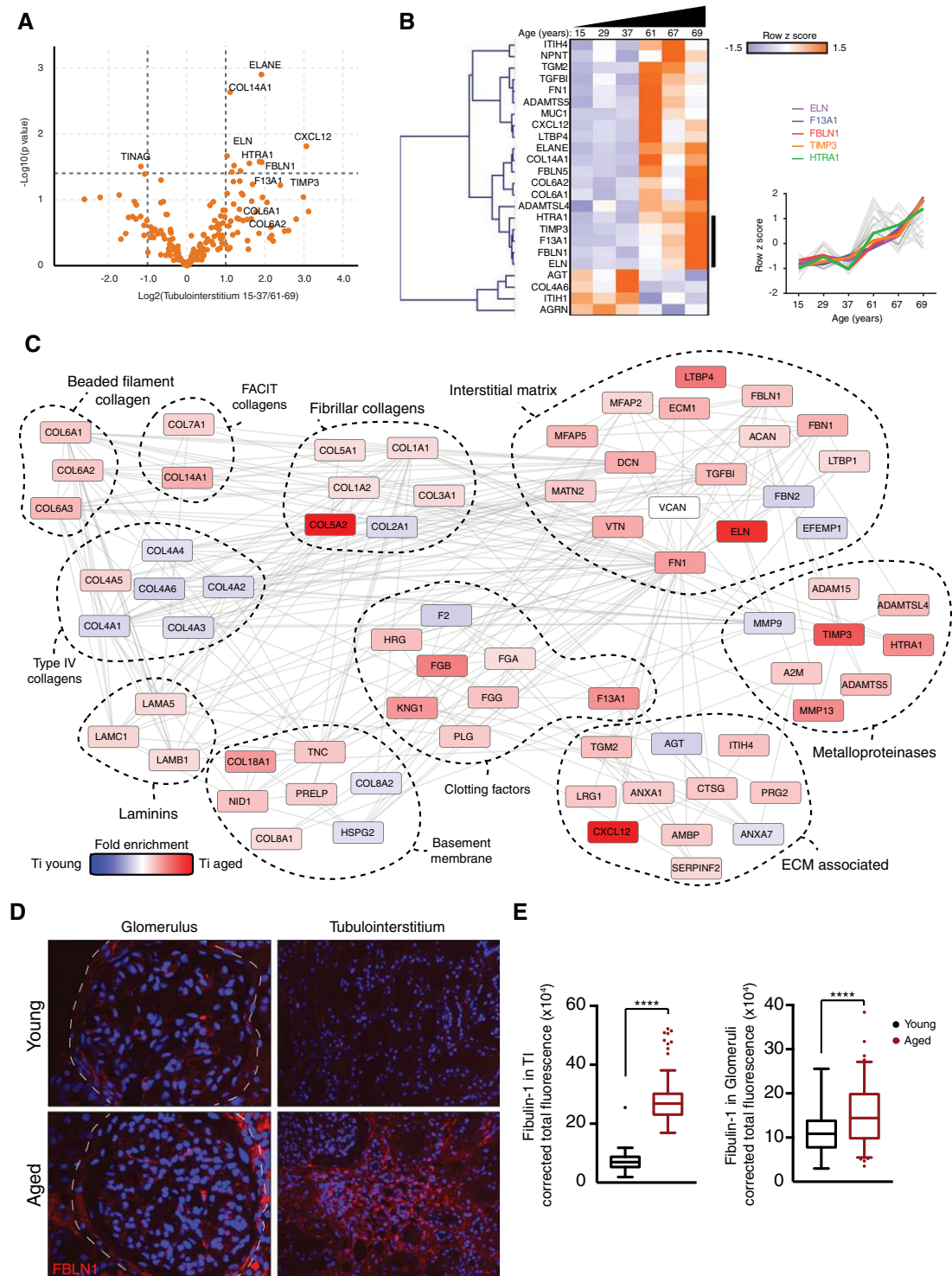


Figure 6. Matrix composition of the human tubulointerstitium changes with age. TI matrix was isolated from young (15, 29, 37 years) and aged (61, 67, 69 years) human kidney samples. (A) Volcano plots of proteins detected in ECM fractions demonstrate differential protein abundance shown as $\log_2(\text{fold change})$ of aged over young TI on the x axis and $-\log_{10}(P \text{ value})$ on the y axis. (B) Unsupervised hierarchical clustered heat map displaying ECM proteins detected in young and aged glomerular datasets. Data were standardized by row z-score and grouped in MeV using Pearson correlation complete-linkage clustering. Inset line graph shows increased collagen VI protein abundance with age. (C) Protein-protein interaction network of altered human TI matrix proteins. Mass spectrometry data from matrix-enriched protein fractions were filtered for known matrix proteins. These proteins were mapped onto a merged human, mouse, and rat interactome. Nodes represent proteins and edges represent reported protein-

highlighted biological processes associated with matrix and adhesion but also with immune system processes. We also compared the matrix signature proteins to RNA levels using the Nephroseq database, and across a variety of phenotypes we observed similar increases in the signature transcripts (Figure 8E and Supplemental Tables 3 and 4). Finally, we combined all primary, processed data from this study to allow direct evaluation (Supplemental Table 5).

DISCUSSION

In this study, we aimed to define altered matrix at the molecular level in kidney aging and disease. We (1) found ultrastructural change in matrix coupled with altered composition in models of glomerular disease; (2) found similar patterns of altered glomerular matrix in human aging, with a reduction in BM proteins and an increase in interstitial matrix; (3) defined the human TI matrix as a network of 141 components, with a distinct pattern of altered matrix in aging; and (4) observed a signature of altered matrix in kidney aging and disease, and provide evidence for shared pathobiology.

The processes that drive abnormal matrix in tissues remain unclear, although this understanding could lead to targeted therapies. In this study, we describe altered matrix structure with evolution over age and disease progression. The GBM of *Col4a3*^{-/-} and *Col4a5*^{-/-} mice at 6–8 weeks appeared normal; however, proteomic analysis identified compositional change at this early stage. With age, these disease models progressed with thickened GBM, and the separation between control and disease matrix composition was more apparent. One aspect of the altered matrix was a reduction in BM components, including collagen IV and laminins. In dynamic studies of endogenously tagged proteins in *Caenorhabditis elegans*, laminin and collagen IV orthologs have slower recovery after photobleaching compared with nidogens, agrin, and perlecan.⁴³ With this in mind, the reduction in BM components we observed could represent damage to these structures and an inability to replenish. We also observed increases of interstitial matrix components nephronectin and collagen VI within the glomerular matrix. Moreover, we identified integration of collagen VI into the GBM in *Col4a3*^{-/-} mice. Genetic variants in *COL6A1/2/3* cause Bethlem and Ulrich myopathies,⁴⁴ but no reported kidney phenotype. However, collagen VI degradation has been associated with CKD,⁴⁵ and its cleavage product, endotrophin, triggers fibrosis and metabolic dysfunction.⁴⁶

Glomerular capillaries are exposed to mechanical load during filtration. Loss of a key BM component may affect the mechanical properties of the GBM. Equally, loss of collagen VI has been shown to alter stiffness in the pericellular matrix of cartilage.⁴⁰ Therefore, collagen VI deposition in aging and disease may occur to restore the mechanical properties of the GBM. Furthermore, collagen VI is a prominent downstream regulator of myofibroblast activity, with knock-down reducing fibrosis.⁴⁷ Our data show collagen VI increasing early, where it may act to strengthen BM defects while, paradoxically, promoting fibrosis (Figure 8E). However, the role of increased collagen VI requires further investigation, as does the potential for targeted inhibition.

In parallel with altered matrix, we observed changes in cell adhesion components. The complex of proteins that assemble upon adhesion receptor and ligand engagement has been described for interactions with fibronectin,²¹ in addition to the BM ligands collagen IV and laminin.⁴⁸ The consensus adhesome identified a series of four signaling hubs,³⁸ and we found a global increase in components across all four signaling hubs. In addition, we found increases in receptors and their paired matrix ligands, including integrin $\alpha1\beta1$, integrin $\alpha2\beta1$ with increased fibrillar collagens (I and III), and collagen VI and integrin $\alpha8\beta1$ with nephronectin. Nephronectin is predominantly localized to the mesangium in the glomerulus and regulates mesangial cell adhesion⁴⁹; however, increased GBM localization of nephronectin is reported in DKD.¹² Our analysis of matrix receptors focused on the integrin adhesion complexes because we did not detect discoid domain receptors or syndecans. This could be due to low abundance or due to factors limiting their detection by mass spectrometry. Overall, the changes we observed in adhesion components could be explained by increased cell-matrix adhesion, associated with podocyte effacement, and increased interaction with the GBM.

To relate our findings in mice to human tissue, we investigated matrix isolated from young and older human kidneys. We also found a reduction in BM components and increased collagen VI and nephronectin in the aged glomerular matrix. Indeed, these components were also increased in proteomic studies of IgA nephropathy¹¹ and DKD,¹² and collagen VI was also upregulated in aged human dentin.^{50(preprint)} A Nephroseq analysis provided further correlation between matrix signature proteins and transcriptional change in a variety of glomerular phenotypes. Kidney disease and aging is associated with altered TI matrix and, therefore, we defined the human TI matrixome. We confirmed localization of 70% of these proteins in

protein interactions. Color represents fold enrichment to datasets, with increased abundance in aged human TI samples illustrated in red, and increased abundance in young human TI samples illustrated in blue. Proteins are grouped functionally. (D) Sections of normal human kidneys were stained with an antibody to fibulin-1 (FBLN1; red) and nuclei were stained with Hoechst 33342 (blue). Representative images are shown. Original magnification, $\times 40$ in left panel; $\times 20$ in right panel. (E) The fluorescent signal in 20 fields per kidney was quantified using ImageJ. *** $P < 0.001$, **** $P < 0.0001$.

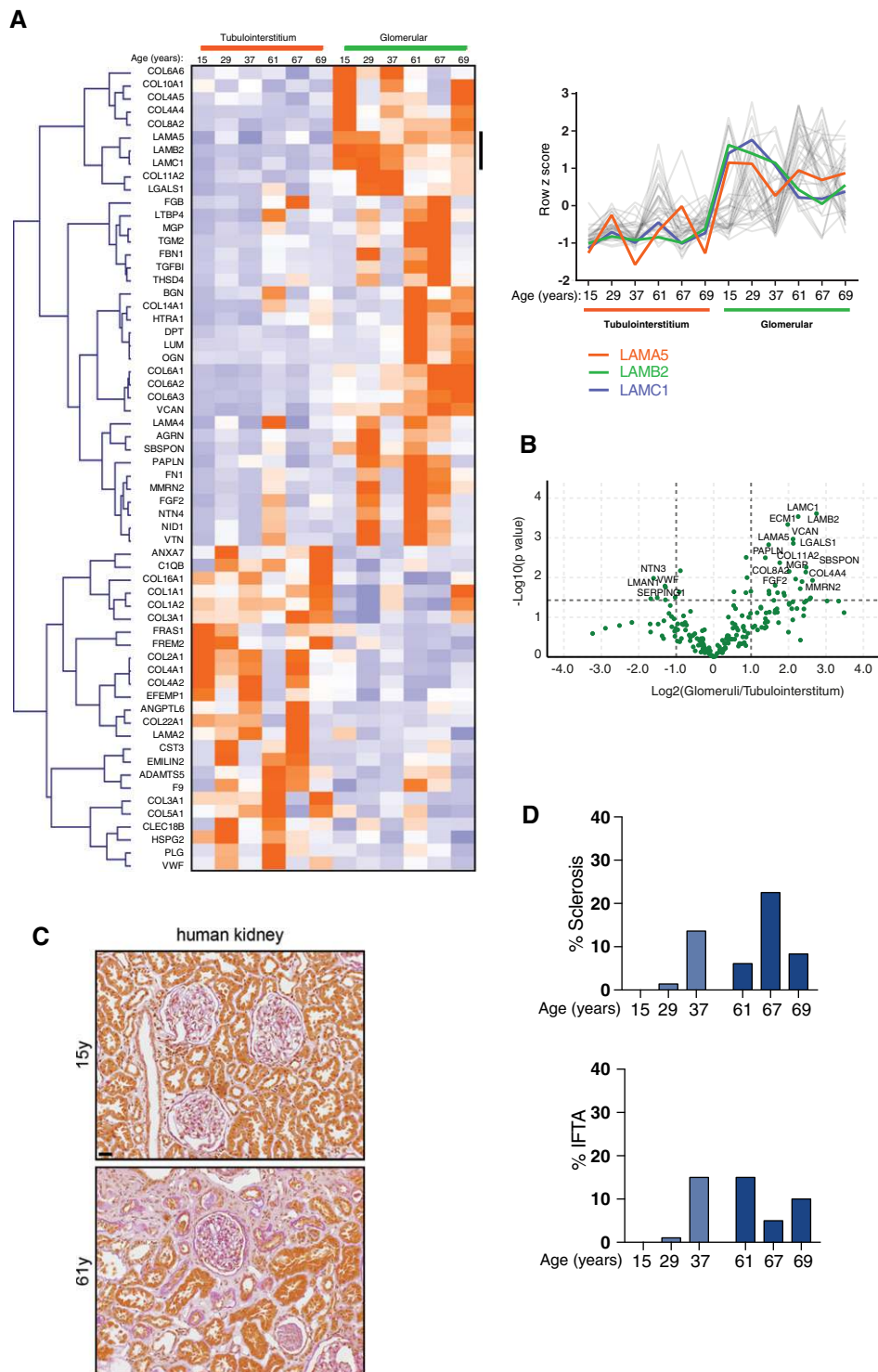


Figure 7. Evidence for distinct age-associated alterations in glomerular compared with TI matrix. (A) Comparison of human glomerular and human TI matrix proteins with age. Unsupervised hierarchical clustered heat map displaying ECM proteins detected in human glomerular and TI samples analyzed by mass spectrometry. Data were standardized by row z-score, clustered using Pearson uncentered distance matrix, and visualized in MeV. Line graphs show laminin proteins, with increased abundance in the human glomerular matrix relative to human TI samples. (B) Volcano plots of proteins detected in ECM fractions demonstrate differential protein abundance shown as $\log_2(\text{fold change})$ of glomerular over tubulointerstitium fractions on the x axis and $-\log_{10}(P \text{ value})$ on the y axis. (C) TriPAS staining of young and older kidney sections highlighting increased matrix in the older kidney section. Scale bar, 100 μm . (D) Glomerulosclerosis and interstitial fibrosis and tubular atrophy (IFTA) scoring in $n=3$ young and $n=3$ aged kidneys.

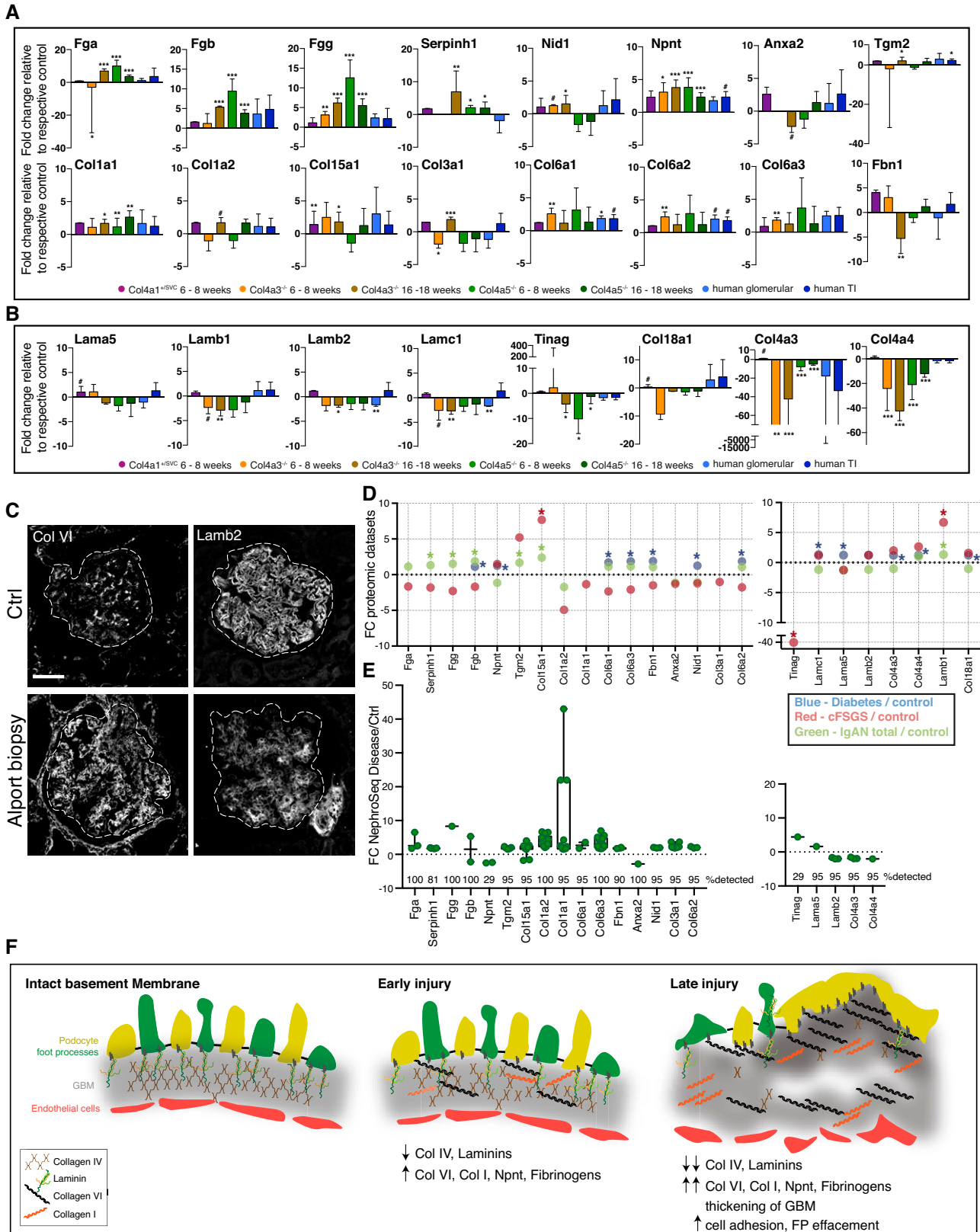


Figure 8. Holistic analysis reveals a signature of altered kidney matrix in aging and disease. (A–B) Bar graphs displaying protein fold change of consistently altered matrix signature proteins relative to their respective controls. Error bars represent SD. [#] $P < 0.1$, ^{*} $P < 0.05$, ^{**} $P < 0.01$, ^{***} $P < 0.001$. (A) Upregulated signature proteins. (B) Downregulated signature proteins. (C) Biopsy sections from a patient with

different kidney matrix compartments, using the Human Protein Atlas, and thereby demonstrate the value of proteomics for increasing the known composition of matrix compartments as an adjunct to immunolocalization. We further examined the change in TI matrix in aging and defined a profile of altered matrix. Interestingly, we did not observe the same reduction in stable BM components seen in the glomerular matrix and hypothesize this is due to differential mechanical load on glomerular and tubular BMs.⁵¹ However, this could also depend on the pathological process, and a reduction of BM components was recently described in a proteomic analysis of transplant kidney rejection.⁵²

In addition to resident kidney cells secreting abnormal matrix, transiting or infiltrating immune cells may also contribute. Macrophage to fibroblast crosstalk has been shown to direct new matrix synthesis, and the direct contribution of macrophages to collagen scar formation in the heart is described in zebrafish.⁵³ Starting with the matrix signature proteins, we identified experimentally confirmed protein interactors and demonstrated three clusters of enriched biological processes. Unsurprisingly, these included cell matrix and cell adhesion, but also processes related to complement, TNF, NF- κ B, and immune response to infection. These findings suggest the signature of an altered matrix has greater interaction with immune system components than previously recognized.

In conclusion, we describe a molecular basis for altered matrix in the kidney, with common features across aging and disease. Further investigations will focus on the cellular origins of the altered matrix and on the role of mechanical load on BM stability.

DISCLOSURES

M.J. Humphries reports having consultancy agreements with Alpha-5; receiving honoraria from the Biotechnology and Biological Sciences Research Council; and serving as a scientific advisor for, or member of, the Biotechnology and Biological Sciences Research Council, *Journal of Cell Biology*, *Journal of Cell Science*, and *Matrix Biology*. R. Lennon reports serving as a trustee for Alport UK and Kidneys for Life; serving on the Scientific Advisor Research Network for the Alport Syndrome Foundation and on the Kidney Research UK grants panel; receiving studentship funding from GlaxoSmithKline; having other interests in/relationships with Kidney Research UK; serving as a consultant for, and having consultancy agreements with, Travers Therapeutics; and receiving funding from the Wellcome Trust. D.A. Long reports serving as an editorial board member of *JASN* and

as an academic editor for *PLOS One*; and having a patent held with UCL Business related to vascular endothelial growth factor C therapy in polycystic kidney disease (JP6261617). J.H. Miner reports having consultancy agreements with Alpha Insights, Bridge Bio, Deerfield Management, Janssen Biotech Inc., Mantra Bio, and The Planning Shop; serving as the president-elect of the American Society for Matrix Biology; having patents and inventions with Angion, Kerfast, and Maze Therapeutics; receiving honoraria from the Japanese Society of Pharmacology and University of Kansas Medical Center; and serving as a consulting editor for the *Journal of Clinical Investigation* and on the editorial board of *Kidney International*, *Matrix Biology*, and *Matrix Biology Plus*. J.T. Norman reports receiving studentship funding from AstraZeneca and UCB; and serving as associate editor for *BMC Nephrology*, associate editor for the *European Journal of Clinical Investigation*, as a committee member of the Kidney Research UK Research Strategy Committee, as a trustee of Kidney Research UK, as a committee member of Medical Research Council Genetically Engineered Mice for Medicine, on the editorial board for *Nature Scientific Reports*, and as co-chair of the UK Renal Fibrosis Network. T. Van Agtmael reports serving on the editorial board of the journal *Bioscience Reports* and the editorial board for the cardiovascular therapeutics section of the journal *Frontiers in Cardiovascular Medicine*. All remaining authors have nothing to disclose.

FUNDING

This work was supported by Wellcome Trust <https://doi.org/10.13039/100004440> Senior Fellowship Award 202860/Z/16/Z (to R. Lennon) and grant 092015 (to M.J. Humphries), Kidney Research UK <https://doi.org/10.13039/501100000291> grant RP52/2014 (awarded to R. Lennon and J.H. Miner to support a postdoctoral research assistant position for M.J. Randles), and Cancer Research UK <https://doi.org/10.13039/501100000289> grant C13329. D.A. Long's laboratory is supported by Medical Research Council <https://doi.org/10.13039/501100000265> grant MR/P018629/1; Diabetes UK <https://doi.org/10.13039/501100000361> grants 13/0004763, 15/0005283, and 17/0005733; Kidney Research UK <https://doi.org/10.13039/501100000291> grant RP36/2015; and by the NIHR Imperial Biomedical Research Centre <https://doi.org/10.13039/501100013342> at Great Ormond Street Hospital for Children <https://doi.org/10.13039/501100003784> University College London Hospitals NHS Foundation Trust <https://doi.org/10.13039/501100008721>. T. Van Agtmael's laboratory is supported by Kidney Research UK <https://doi.org/10.13039/501100000291> grant RP 19/2012, British Heart Foundation <https://doi.org/10.13039/501100000274> grant PG/15/92/31813, and Medical Research Council <https://doi.org/10.13039/501100000265> grant MR/R005567-1. The authors also acknowledge Wellcome Trust <https://doi.org/10.13039/100004440> core funding under grant 203128/Z/16/Z to the Wellcome Centre for Cell-Matrix Research at the University of Manchester.

ACKNOWLEDGMENTS

Mass spectrometry was performed in the Biomolecular Analysis Core Facility, Faculty of Life Sciences, University of Manchester, and we thank

autosomal recessive Alport syndrome and control (Ctrl) kidney tissue (nonaffected tissue of a tumor nephrectomy sample) Background was subtracted from immunofluorescence images using a rolling-ball algorithm in ImageJ. C were stained for type VI collagen (Col VI), laminin- β 2 (Lamb2). Scale bar, 50 μ m. (D) Dot plot comparison of signature matrix proteins to their protein levels in microdissected human IgA nephropathy (IgAN) samples (IgAN total and progressive IgAN),¹¹ human diabetic samples,¹² and human FSGS samples (collapsing FSGS [cFSGS] and FSGS not otherwise specified).⁴² Fold change (FC) is presented on the y axis and dataset is highlighted by color. * $P < 0.05$. (E) Analysis of signature protein transcript levels in different disease datasets using the Nephroseq version 5 database. Glomerular datasets were extracted and altered transcript levels with fold change ± 1.5 and $P < 0.05$ are shown. The percentage detection of searched gene transcript is shown (number of datasets = 21). Full details for Nephroseq datasets and transcript fold changes used for each signature gene can be found in Supplemental Table 3. (F) Schematic of hypothesized BM injury process. FP, foot process.

Dr. David Knight and Dr. Stacey Warwood for advice and technical support and Mr. Julian Selley for bioinformatic support. Special thanks goes to Dr. Peter March and Mr. Roger Meadows for their help with the microscopy. The authors thank the staff in the Electron Microscopy Core Facility in the Faculty of Biology, Medicine and Health for their assistance. Special thanks goes to Dr. Aleksandr Mironov and Dr. Tobias Starborg and the Wellcome Trust for equipment grant support to the Electron Microscopy Core Facility.

The mass spectrometer and microscopes used in this study were purchased with grants from the Biotechnology and Biological Sciences Research Council, the Wellcome Trust, and the University of Manchester Strategic Fund.

R. Lennon, M.J. Randles, J.H. Miner, T. Von Agtmael, J.T. Norman, D.A. Long, P. Potter, and M.J. Humphries conceived and designed the studies; M.J. Randles, F. Lausecker, Q. Kong, M. Kolatsi-Joannou, P. Tian, and S. Falcone acquired the data; G. Reid performed histologic analysis on kidney sections; and all authors played an important role in interpreting the results, and in drafting and revising the manuscript. The authors have full access to the data in the study.

DATA SHARING STATEMENT

The proteomics data were deposited in the ProteomeXchange Consortium⁵⁴ via the Proteomics Identifications Database partner repository with the dataset identifier PXD022363 (Col4a1 mouse glomerular datasets), PXD022392 (Col4a3 mouse glomerular datasets), PXD022227 (Col4a5 mouse glomerular ECM and cellular fraction), and PXD022219 (human kidney proteomics, glomerular, tubular, cellular, and matrix fractions).

SUPPLEMENTAL MATERIAL

This article contains the following supplemental material online at <http://jasn.asnjournals.org/lookup/suppl/doi:10.1681/ASN.2020101442/-/DCSupplemental>.

Supplemental Figure 1. Glomerular localization of type IV collagen isoforms.

Supplemental Figure 2. Characterization of *Col4a5*^{-/-} mice.

Supplemental Figure 3. Overview of glomerular proteomic data.

Supplemental Figure 4. Altered matrixome proteins in *Col4a* mice

Supplemental Figure 5. Altered matrixome proteins in *Col4a3*^{-/-} mice.

Supplemental Figure 6. Altered matrixome proteins in *Col4a5*^{-/-} mice.

Supplemental Figure 7. Human kidney data enrichment analysis.

Supplemental Figure 8. Defining the tubulointerstitial matrixome

Supplemental Figure 9. Identification of new tubulointerstitial matrix proteins.

Supplemental Figure 10. Defining the human kidney extracellular matrix.

Supplemental Figure 11. One-hop interactors of the upregulated matrix signature proteins.

Supplemental Video 1. SV1-Col4a1-16weeks.

Supplemental Video 2. SV2-Col4a3-16weeks.

Supplemental Video 3. SV3-Col4a3-28weeks.

Supplemental Video 4. SV4-Col4a5-16weeks.

Supplemental Table 1. Abundance of matrix proteins in mouse models.

Supplemental Table 2. This is in the methods section Mass Spectrometry Quantification.

Supplemental Table 3. Nephroseq v5 analysis.

Supplemental Table 4. Human disease comparison.

Supplemental Table 5. Normalized abundance for all primary datasets.

REFERENCES

- Yurchenco PD: Basement membranes: Cell scaffoldings and signaling platforms. *Cold Spring Harb Perspect Biol* 3: a004911, 2011
- Li X, Chen Y, Schéeele S, Arman E, Haffner-Krausz R, Ekblom P, et al.: Fibroblast growth factor signaling and basement membrane assembly are connected during epithelial morphogenesis of the embryoid body. *J Cell Biol* 153: 811–822, 2001
- Naba A, Clauser KR, Hoersch S, Liu H, Carr SA, Hynes RO: The matrixome: *In silico* definition and *in vivo* characterization by proteomics of normal and tumor extracellular matrices. *Mol Cell Proteomics* 11: M111.014647, 2012
- Wynn TA: Cellular and molecular mechanisms of fibrosis. *J Pathol* 214: 199–210, 2008
- Haas M, Rastaldi MP, Fervenza FC: Histologic classification of glomerular diseases: Clinicopathologic correlations, limitations exposed by validation studies, and suggestions for modification [published correction appears in *Kidney Int* 86: 648, 2014 10.1038/ki.2014.230]. *Kidney Int* 85: 779–793, 2014
- Remuzzi G, Bertani T: Is glomerulosclerosis a consequence of altered glomerular permeability to macromolecules? *Kidney Int* 38: 384–394, 1990
- Zeisberg M, Neilson EG: Mechanisms of tubulointerstitial fibrosis. *J Am Soc Nephrol* 21: 1819–1834, 2010
- O’Sullivan ED, Hughes J, Ferenbach DA: Renal aging: Causes and consequences. *J Am Soc Nephrol* 28: 407–420, 2017
- Lennon R, Byron A, Humphries JD, Randles MJ, Carisey A, Murphy S, et al.: Global analysis reveals the complexity of the human glomerular extracellular matrix. *J Am Soc Nephrol* 25: 939–951, 2014
- Hobeika L, Barati MT, Caster DJ, McLeish KR, Merchant ML: Characterization of glomerular extracellular matrix by proteomic analysis of laser-captured microdissected glomeruli. *Kidney Int* 91: 501–511, 2017
- Paunas FTI, Finne K, Leh S, Osman TA, Marti HP, Berven F, et al.: Characterization of glomerular extracellular matrix in IgA nephropathy by proteomic analysis of laser-captured microdissected glomeruli. *BMC Nephrol* 20: 410, 2019
- Nakatani S, Wei M, Ishimura E, Kakehashi A, Mori K, Nishizawa Y, et al.: Proteome analysis of laser microdissected glomeruli from formalin-fixed paraffin-embedded kidneys of autopsies of diabetic patients: Nephronectin is associated with the development of diabetic glomerulosclerosis. *Nephrol Dial Transplant* 27: 1889–1897, 2012
- Randles MJ, Humphries MJ, Lennon R: Proteomic definitions of basement membrane composition in health and disease. *Matrix Biol* 57–58: 12–28, 2017
- Miner JH: Renal basement membrane components. *Kidney Int* 56: 2016–2024, 1999
- Khoshnoodi J, Pedchenko V, Hudson BG: Mammalian collagen IV. *Microsc Res Tech* 71: 357–370, 2008
- Van Agtmael T, Schlötzer-Schrehardt U, McKie L, Brownstein DG, Lee AW, Cross SH, et al.: Dominant mutations of Col4a1 result in basement membrane defects which lead to anterior segment dysgenesis and glomerulopathy. *Hum Mol Genet* 14: 3161–3168, 2005
- Miner JH, Sanes JR: Molecular and functional defects in kidneys of mice lacking collagen alpha 3(IV): Implications for Alport syndrome. *J Cell Biol* 135: 1403–1413, 1996
- Dickinson ME, Flenniken AM, Ji X, Teboul L, Wong MD, White JK, et al.; International Mouse Phenotyping Consortium; Jackson Laboratory; Infrastructure Nationale PHENOMIN, Institut Clinique de la Souris (ICS); Charles River Laboratories; MRC Harwell; Toronto Centre for Phenogenomics; Wellcome Trust Sanger Institute; RIKEN BioResource Center: High-throughput discovery of novel developmental phenotypes. *Nature* 537: 508–514, 2016
- IMP C: Allele Col4a5 tm1b (EUCOMM)Wtsi, Available at: Meehan, T. F. et al. Disease model discovery from 3,328 gene knockouts by the International Mouse Phenotyping Consortium. *Nat. Genet.* 49, (2017).
- Shevchenko A, Wilm M, Vorm O, Mann M: Mass spectrometric sequencing of proteins silver-stained polyacrylamide gels. *Anal Chem* 68: 850–858, 1996

21. Humphries JD, Byron A, Bass MD, Craig SE, Pinney JW, Knight D, et al.: Proteomic analysis of integrin-associated complexes identifies RCC2 as a dual regulator of Rac1 and Arf6. *Sci Signal* 2: ra51, 2009
22. Nesvizhskii AI, Keller A, Kolker E, Aebersold R: A statistical model for identifying proteins by tandem mass spectrometry. *Anal Chem* 75: 4646–4658, 2003
23. Zaidel-Bar R, Geiger B: The switchable integrin adhesome. *J Cell Sci* 123: 1385–1388, 2010
24. Berthier CC, Bethunaickan R, Gonzalez-Rivera T, Nair V, Ramanujam M, Zhang W, et al.: Cross-species transcriptional network analysis defines shared inflammatory responses in murine and human lupus nephritis. *J Immunol* 189: 988–1001, 2012
25. Hodgkin JB, Nair V, Zhang H, Randolph A, Harris RC, Nelson RG, et al.: Identification of cross-species shared transcriptional networks of diabetic nephropathy in human and mouse glomeruli. *Diabetes* 62: 299–308, 2013
26. Hodgkin JB, Borczuk AC, Nasr SH, Markowitz GS, Nair V, Martini S, et al.: A molecular profile of focal segmental glomerulosclerosis from formalin-fixed, paraffin-embedded tissue. *Am J Pathol* 177: 1674–1686, 2010
27. Ju W, Greene CS, Eichinger F, Nair V, Hodgkin JB, Bitzer M, et al. Defining cell-type specificity at the transcriptional level in human disease. *Genome Res* 23: 1862–1873, 2013
28. Neusser MA, Lindenmeyer MT, Moll AG, Segerer S, Edenhofer I, Sen K, et al.: Human nephrosclerosis triggers a hypoxia-related glomerulopathy. *Am J Pathol* 176: 594–607, 2010
29. Peterson KS, Huang JF, Zhu J, D'Agati V, Liu X, Miller N, et al.: Characterization of heterogeneity in the molecular pathogenesis of lupus nephritis from transcriptional profiles of laser-captured glomeruli. *J Clin Invest* 113: 1722–1733, 2004
30. Reich HN, Tritschler D, Cattran DC, Herzenberg AM, Eichinger F, Boucherot A, et al.: A molecular signature of proteinuria in glomerulonephritis. *PLoS One* 5: e13451, 2010
31. Woroniecka KI, Park AS, Mohtat D, Thomas DB, Pullman JM, Susztak K: Transcriptome analysis of human diabetic kidney disease. *Diabetes* 60: 2354–2369, 2011
32. Starborg T, Kalson NS, Lu Y, Mironov A, Cootes TF, Holmes DF, et al.: Using transmission electron microscopy and 3View to determine collagen fibril size and three-dimensional organization. *Nat Protoc* 8: 1433–1448, 2013
33. Jones FE, Murray LS, McNeilly S, Dean A, Aman A, Lu Y, et al.: 4-Sodium phenyl butyric acid has both efficacy and counter-indicative effects in the treatment of Col4a1 disease. *Hum Mol Genet* 28: 628–638, 2019
34. Suleiman H, Zhang L, Roth R, Heuser JE, Miner JH, Shaw AS, et al.: Nanoscale protein architecture of the kidney glomerular basement membrane. *eLife* 2: e01149, 2013
35. Suleiman HY, Roth R, Jain S, Heuser JE, Shaw AS, Miner JH: Injury-induced actin cytoskeleton reorganization in podocytes revealed by super-resolution microscopy. *JCI Insight* 2: e94137, 2017
36. Jones FE, Bailey MA, Murray LS, Lu Y, McNeilly S, Schlötzer-Schrehardt U, et al.: ER stress and basement membrane defects combine to cause glomerular and tubular renal disease resulting from Col4a1 mutations in mice. *Dis Model Mech* 9: 165–176, 2016
37. Tsuji K, Suleiman H, Miner JH, Daley JM, Capen DE, Păunescu TG, et al.: Ultrastructural characterization of the glomerulopathy in Alport mice by helium ion scanning microscopy (HIM). *Sci Rep* 7: 11696, 2017
38. Horton ER, Byron A, Askari JA, Ng DHJ, Millon-Frémillon A, Robertson J, et al.: Definition of a consensus integrin adhesome and its dynamics during adhesion complex assembly and disassembly. *Nat Cell Biol* 17: 1577–1587, 2015
39. Zhou XJ, Saxena R, Liu Z, Vaziri ND, Silva FG: Renal senescence in 2008: progress and challenges. *Int Urol Nephrol* 40: 823–839, 2008
40. Alexopoulos LG, Youn I, Bonaldo P, Guilak F: Developmental and osteoarthritic changes in Col6a1-knockout mice: biomechanics of type VI collagen in the cartilage pericellular matrix. *Arthritis Rheum* 60: 771–779, 2009
41. Uhlen M, Oksvold P, Fagerberg L, Lundberg E, Jonasson K, Forsberg M, et al.: Towards a knowledge-based Human Protein Atlas. *Nat Biotechnol* 28: 1248–1250, 2010
42. Merchant ML, Barati MT, Caster DJ, Hata JL, Hobeika L, Coventry S, et al.: Proteomic analysis identifies distinct glomerular extracellular matrix in collapsing focal segmental glomerulosclerosis. *J Am Soc Nephrol* 31: 1883–1904, 2020
43. Keeley DP, Hastie E, Jayadev R, Kelley LC, Chi Q, Payne SG, et al.: Comprehensive endogenous tagging of basement membrane components reveals dynamic movement within the matrix scaffolding. *Dev Cell* 54: 60–74.e7, 2020
44. Bönnemann CG: The collagen VI-related myopathies Ullrich congenital muscular dystrophy and Bethlem myopathy. *Handb Clin Neurol* 101: 81–96, 2011
45. Rasmussen DGK, Boesby L, Nielsen SH, Tepel M, Birot S, Karsdal MA, et al.: Collagen turnover profiles in chronic kidney disease. *Sci Rep* 9: 16062, 2019
46. Sun K, Park J, Gupta OT, Holland WL, Auerbach P, Zhang N, et al.: Endotrophin triggers adipose tissue fibrosis and metabolic dysfunction. *Nat Commun* 5: 3485, 2014
47. Williams LM, McCann FE, Cabrita MA, Layton T, Cribbs A, Knezevic B, et al.: Identifying collagen VI as a target of fibrotic diseases regulated by CREBBP/EP300. *Proc Natl Acad Sci U S A* 117: 20753–20763, 2020
48. Randles MJ, Lausecker F, Humphries JD, Byron A, Clark SJ, Miner JH, et al.: Basement membrane ligands initiate distinct signalling networks to direct cell shape. *Matrix Biol* 90: 61–78, 2020
49. Zimmerman SE, Hiremath C, Tsunetzumi J, Yang Z, Finney B, Marciano DK: Nephronectin regulates mesangial cell adhesion and behavior in glomeruli. *J Am Soc Nephrol* 29: 1128–1140, 2018
50. Reis M, Lee F, Bedran-Russo AK, Naba A: Proteomic profiling of the human dentin identifies age-related differences in the composition and solubility of the matrixome. *BioRxiv* (Preprint posted December 4, 2020)
51. Kriz W, Lemley KV: A potential role for mechanical forces in the detachment of podocytes and the progression of CKD. *J Am Soc Nephrol* 26: 258–269, 2015
52. Clotet-Freixas S, McEvoy CM, Batruch I, Pastrello C, Kotlyar M, Van JAD, et al.: Extracellular matrix injury of kidney allografts in antibody-mediated rejection: A proteomics study. *J Am Soc Nephrol* 31: 2705–2724, 2020
53. Simões FC, Cahill TJ, Kenyon A, Gavriouchkina D, Vieira JM, Sun X, et al.: Macrophages directly contribute collagen to scar formation during zebrafish heart regeneration and mouse heart repair. *Nat Commun* 11: 600, 2020
54. Vizcaino JA, Csordas A, Del-Toro N, Dianes JA, Griss J, Lavidas I, et al.: 2016 update of the PRIDE database and its related tools [published correction appears in *Nucleic Acids Res* 44: 11033, 2016 10.1093/nar/gkw880]. *Nucleic Acids Res* 44: D447–D456, 2016

See related editorial “Too Little or Too Much? Extracellular Matrix Remodeling in Kidney Health and Disease”. on pages 1541–1543.

AFFILIATIONS

¹Wellcome Centre for Cell-Matrix Research, Division of Cell-Matrix Biology and Regenerative Medicine, School of Biological Sciences, Faculty of Biology Medicine and Health, The University of Manchester, Manchester Academic Health Science Centre, Manchester, United Kingdom

²Department of Renal Medicine, University College London, London, United Kingdom

³Renal Division, Washington University School of Medicine, Saint Louis, Missouri

⁴Department of Histopathology, Manchester Royal Infirmary, Manchester University Hospitals National Health Service Foundation Trust, Manchester Academic Health Science Centre, Manchester, United Kingdom

⁵Developmental Biology and Cancer Programme, Great Ormond Institute of Child Health, University College London, London, United Kingdom

⁶Centre for Cellular and Molecular Physiology, University of Oxford, Oxford, United Kingdom

⁷Department Biological and Medical Sciences, Faculty of Health and Life Sciences, Oxford Brookes University, Oxford, United Kingdom

⁸Institute of Cardiovascular and Medical Sciences, University of Glasgow, Glasgow, United Kingdom

⁹Department of Paediatric Nephrology, Royal Manchester Children's Hospital, Manchester University Hospitals National Health Service Foundation Trust, Manchester Academic Health Science Centre, Manchester, United Kingdom